

www.acsami.org Research Article

# Sub-100 mA/cm<sup>2</sup> CO<sub>2</sub>-to-CO Reduction Current Densities in Hierarchical Porous Gold Electrocatalysts Made by Direct Ink Writing and Dealloying

Jintao Fu, Shahryar Mooraj, Alexander K. Ng, Cheng Zhu, Wen Chen, and Eric Detsi\*



Cite This: ACS Appl. Mater. Interfaces 2023, 15, 27905-27914



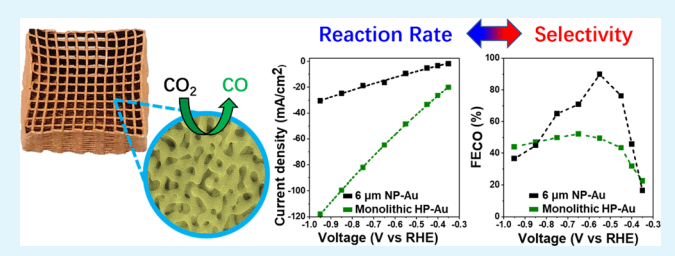
**ACCESS** I

III Metrics & More

Article Recommendations

Supporting Information

**ABSTRACT:** While most research efforts on  $CO_2$ -to-CO reduction electrocatalysts focus on boosting their selectivity, the reduction rate, directly proportional to the reduction current density, is another critical parameter to be considered in practical applications. This is because mass transport associated with the diffusion of reactant/product species becomes a major concern at a high reduction rate. Nanostructured Au is a promising  $CO_2$ -to-CO reduction electrocatalyst for its very high selectivity. However, the  $CO_2$ -to-CO reduction current density commonly achieved in



conventional nanostructured Au electrocatalysts is relatively low (in the range of  $1-10~\text{mA/cm}^2$ ) for practical applications. In this work, we combine direct ink writing-based additive manufacturing and dealloying to design a robust hierarchical porous Au electrocatalyst to improve the mass transport and achieve high  $\text{CO}_2$ -to-CO reduction current densities on the order of 64.9 mA/cm² with CO partial current density of 33.8 mA/cm² at 0.55 V overpotential using an H-cell configuration. Although the current density achieved in our robust hierarchical porous Au electrocatalyst is one order of magnitude higher than the one achieved in conventional nanostructured electrocatalysts, we found that the selectivity of our system is relatively low, namely 52%, which suggests that mass transport remains a critical issue despite the hierarchical porous architecture. We further show that the bulk dimension of our electrocatalyst is a critical parameter governing the interplay between selectivity and reduction rate. The insights gained in this work shed new light on the design of electrocatalysts toward scale-up  $\text{CO}_2$  reduction and beyond.

KEYWORDS: carbon dioxide reduction, hierarchical porous electrocatalyst, nanoporous gold, dealloying, additive manufacturing, direct ink writing

### 1. INTRODUCTION

Reducing carbon dioxide (CO<sub>2</sub>) into value-added carbon species using heterogenous electrocatalysts is a promising approach to cut down greenhouse gas emissions and mitigate climate change. Among electrocatalytic CO<sub>2</sub> reduction (ECR) pathways, the reduction of CO<sub>2</sub> to carbon monoxide (CO) is particularly attractive because CO is used in industry for the manufacturing of various bulk chemicals. Since CO<sub>2</sub>-to-CO reduction often takes place in aqueous solutions, it is accompanied by a competing and undesirable hydrogen evolution reaction (HER).3 Early studies have identified efficient electrocatalysts including Au, Ag, and Zn, which exhibit a high selectivity (ca. 80-85%) toward CO<sub>2</sub>-to-CO reduction in the bulk form. 4 To further improve this selectivity, nanostructured materials with high surface-to-volume ratios have been widely used owing to their abundant surface catalytic sites compared to their bulk counterparts.<sup>5</sup> The density of active catalytic sites can be further maximized by tuning the facets, <sup>6,7</sup> defects, <sup>8,9</sup> and chemical composition <sup>10</sup> of these catalysts. As a result, very high selectivities of up to  $\approx$ 99% for Au,  $^{11,12}$   $\approx$ 95% for Ag,  $^{13,14}$  and  $\approx$ 95% for Zn $^{15,16}$  have been achieved with acceptable overpotentials, usually below 0.5 V

for Au and Ag, and 1.0 V for Zn. Aside from the selectivity, the reaction rate of ECR (usually expressed in terms of current density) is another critical factor to be considered. For practical industrial production of CO from CO<sub>2</sub>, it is desirable to achieve current densities >200 mA/cm<sup>2</sup> with selectivity >95%, corresponding to a CO partial current density of >190 mA/cm<sup>2</sup> (i.e., 200 mA/cm<sup>2</sup> × 0.95). <sup>17,18</sup> However, low CO partial current densities in the range of 1–10 mA/cm<sup>2</sup> are commonly reported in the literature when nanostructured materials including nanoparticles, <sup>11</sup> nanorods, <sup>19</sup> nanosheets, <sup>20</sup> and nanoporous metals <sup>21</sup> are used in H-cell configurations. These low current densities are justified by the relatively small amount of electrocatalysts used to minimize mass transport limitations and maximize selectivity. Consequently, there is still

Received: February 13, 2023 Accepted: April 28, 2023 Published: June 5, 2023





a research gap between the performance metrics of CO<sub>2</sub>-to-CO electrocatalysts at the lab scale  $(1-10 \text{ mA/cm}^2)$  and industrial requirement (>190 mA/cm<sup>2</sup>). This gap can be closed by investigating the performance of robust electrocatalysts with high mass loading. However, increasing the mass loading of electrocatalysts by randomly stacking a large quantity of nanostructured materials is obviously not an ideal approach because issues related to the sluggish mass transport kinetics associated with robust electrodes will diminish the catalyst performance and selectivity. Instead of randomly stacking electrocatalysts, a more holistic approach is needed to design electrocatalysts with engineered architecture to facilitate mass transport. To this end, here we use an additive manufacturing technique based on direct ink writing in combination with dealloying to print robust 3D multiscale, hierarchical porous Au (HP-Au) electrocatalysts, which allows for achieving a high total current density of 64.9 mA/cm<sup>2</sup> with CO partial current density of 33.8 mA/cm<sup>2</sup> at  $\approx$ 0.55 V overpotential, thus yielding 52% selectivity. This current density is one order of magnitude higher than those achieved in conventional nanostructured materials. Despite the hierarchical architecture design, the 52% selectivity of our robust electrocatalyst is significantly lower than the 99% selectivity achievable in conventional nanostructured Au, suggesting that mass transport remains a critical issue. Therefore, the interplay between current density and selectivity is further investigated, and we show that reducing the bulk dimension of electrocatalysts can result in ≈40% improved selectivity (from 52 to 90%), with a trade-off of ≈75% decreased CO partial current density (from 33.8 to 8.4 mA/cm<sup>2</sup>). The insights gained in this study will pave the way for the development of robust electrocatalysts for the largescale reduction of CO<sub>2</sub> to CO and beyond.

# 2. EXPERIMENTAL

- **2.1. Materials Fabrication.** Two types of porous Au samples were fabricated to compare their ECR performance: HP-Au made by direct ink writing and dealloying, and  $\approx 6~\mu$ m-thick nanoporous Au (NP-Au) films made by dealloying commercial gold-silver (Au-Ag) foils with thickness  $\approx 6~\mu$ m (Sepp Leaf Products). Below are further details on the preparation of these two types of samples.
- 2.1.1. Direct Ink Writing. Au-Ag composite inks were prepared by mixing 7 g of Ag clay (90 wt % Ag powder + 10 wt % water and organic binder; precious metal clay (PMC), Mitsubishi Materials) and 6 g of Au clay (91.7 wt % pure Au + 8.3 wt % water and organic binder; PMC, Mitsubishi Materials) with 0.5 to 1.0 g of organic solvent (PasteMaker, Sherri Haab), corresponding to an average of 70 at.% Ag to 30 at.% Au composition. The alloy components were mixed in a planetary centrifugal mixer (Thinky) for 1 min. To create 3D architectures, the ink was loaded into a 3 mL syringe-barrel connected via a Luer-Lok to a tapered nozzle with a 200 µm inner diameter. The print head was pressurized using an air-powered fluid dispenser (Ultimus V, Nordson EFD) to provide the appropriate pressure to extrude the ink through the nozzle.
- 2.1.2. Sintering. The 3D printed Au-Ag alloy samples were sintered and homogenized by annealing them in air in a Vulcan 3–550 programmable furnace (Neytech) at a temperature of 850 °C for 12 h. The diffusion length, L, was estimated using Fick's law,  $L=(2D \cdot t)^{1/2}$ , where D is the diffusion coefficient and t is the diffusion time in seconds. Here,  $D=D_0 \times \exp(-E_a/RT)$ , where  $D_0$  is the temperature-independent diffusion coefficient (cm²/s),  $E_a$  is the activation energy for diffusion (kcal/mol), R is the ideal gas constant [J/(mol K)], and  $E_a$  is the absolute temperature (K). Using reported values for  $E_a$ 0 and  $E_a$ 1 and  $E_a$ 2 and  $E_a$ 3 and  $E_a$ 4 and  $E_a$ 5 kcal/mol for the diffusion of Ag in Au and  $E_a$ 6 and  $E_a$ 7 and  $E_a$ 8 and  $E_a$ 9 at 850 °C for 12 h is calculated to be 80 and 57  $\mu$ m, respectively.

This is well above the Au and Ag particle size of 10 to 20  $\mu$ m used in this work. Thus, the selected annealing protocol should produce a homogeneous alloy.

- 2.1.3. Dealloying. Ag was selectively removed from the Au-Ag alloy precursors by free corrosion dealloying in 15 M nitric acid (HNO<sub>3</sub>) inside a fume hood. The 3D printed Au-Ag precursor alloys were fully dealloyed in 144 h (6 days) with refreshing the acid every 24 h, while the 6  $\mu$ m-thick Au-Ag precursors were dealloyed within 7 h. After dealloying, the corresponding HP-Au and NP-Au samples were rinsed multiple times with deionized (DI) water and kept in DI H<sub>2</sub>O for at least 12 h to thoroughly remove residual acid from the pores. Finally, the samples were dried under vacuum at room temperature and stored inside an Argon-filled glovebox.
- **2.2. Structural Characterization.** A JEOL 7500F scanning electron microscope (SEM) equipped with energy-dispersive X-ray spectroscopy (EDS) was used to obtain the morphology and composition of as-printed, sintered, and dealloyed samples. X-ray diffraction (XRD) patterns were collected using a Rigaku Miniflex powder diffractometer (Cu X-ray source, operated at 40 kV/15 mA) with a 0.02° step size and a 3 °/min scanning speed to investigate the crystal structure of the fabricated materials. Small-angle X-ray scattering (SAXS) was performed using a XENOCS Xeuss 2.0 Environmental X-ray scattering facility with dual copper and molybdenum X-ray sources at Penn, which has a detection limit between 1 Å and 570 nm, to investigate the sizes of the nanoscale ligaments and pores in the fabricated materials. Second 1.
- **2.3. Electrochemical Characterization.** All electrochemical characterizations were performed using a Biologic SP-300 and an Admiral Squidstat potentiostat. Silver/silver chloride (Ag/AgCl) and mercury/mercury oxide (Hg/HgO) were used as reference electrodes depending on the pH of the electrolyte. The measured potentials were converted to a reversible hydrogen electrode (RHE) using:

$$E \text{ (versus RHE)} = E \text{ (versus Ag/AgCl)} + 0.222 \text{ V} + 0.059 \text{ V}$$
 
$$\times \text{pH}$$

$$E \text{ (versus RHE)} = E \text{ (versus Hg/HgO)} + 0.140 \text{ V} + 0.059 \text{ V}$$
$$\times \text{pH}$$

- 2.3.1. Electrode Preparation. Three types of electrodes were investigated to compare the ECR performance: Monolithic HP-Au made by 3D printing and dealloying as described above, HP-Au slurry electrode, and monolithic 6  $\mu$ m-thick NP-Au film also made by dealloying. To prepare the HP-Au slurry electrode, monolithic HP-Au from 3D printing and dealloying was hand-ground into fine powders using a mortar and pestle and mixed with conductive carbon and polyvinylidene fluoride (PVDF) binder (mass ratio 8:1:1), then dried under vacuum at room temperature.
- 2.3.2. Cyclic Voltammetry (CV). CV experiments were performed in 0.5 M H<sub>2</sub>SO<sub>4</sub> solution with HP-Au and NP-Au samples used as the working electrode, a Pt wire as the counter electrode, and Ag/AgCl as the reference electrode. Subsequently, the electrochemical active surface area (EASA) was derived using the ratio of reduced charge density between HP-Au and a planar Au foil at the same scan rate.<sup>29</sup>
- 2.3.3. Lead Underpotential Deposition (Pb-UPD). To investigate the density of active facets present in our materials, Pb-UPD was carried out at the scan rate of 20 mV/s using an Argon-saturated electrolyte consisting of 0.1 M NaOH + 1 mM Pb(ClO<sub>4</sub>)<sub>2</sub>, with HP-Au or NP-Au samples used as the working electrode, a Pt wire as the counter electrode, and Hg/HgO as the reference electrode.<sup>30</sup>
- 2.3.4. Electrocatalytic  $CO_2$  Reduction.  $CO_2$  reduction was performed at room temperature in a gas-sealed H-cell consisting of two compartments separated by an anion exchange membrane (AEM) purchased from Dioxide Materials. Each H-cell compartment was filled with 40 mL 0.5 M KHCO<sub>3</sub> and 25 mL head space was left. A Pt wire was used as the counter electrode in one compartment. In the other compartment, HP-Au or NP-Au was used as the working electrode and Ag/AgCl as the reference electrode. The electrolyte in this latter compartment was saturated with  $CO_2$  (pH = 7.2) at a flow

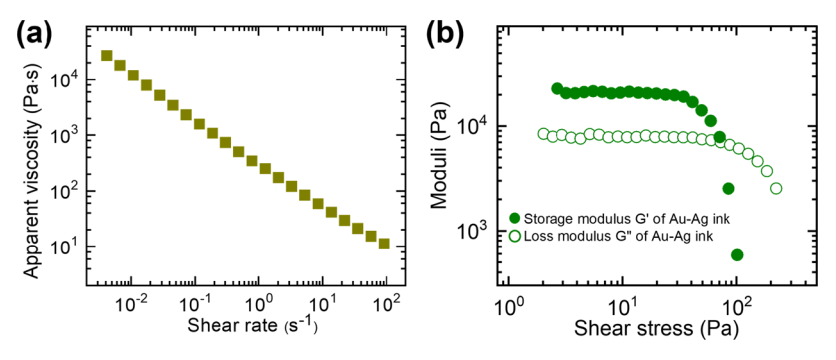


Figure 1. Log-log plots of (a) apparent viscosity as a function of shear rate, and (b) storage (G') and loss (G'') modulus as a function of the shear stress of the Au-Ag ink.

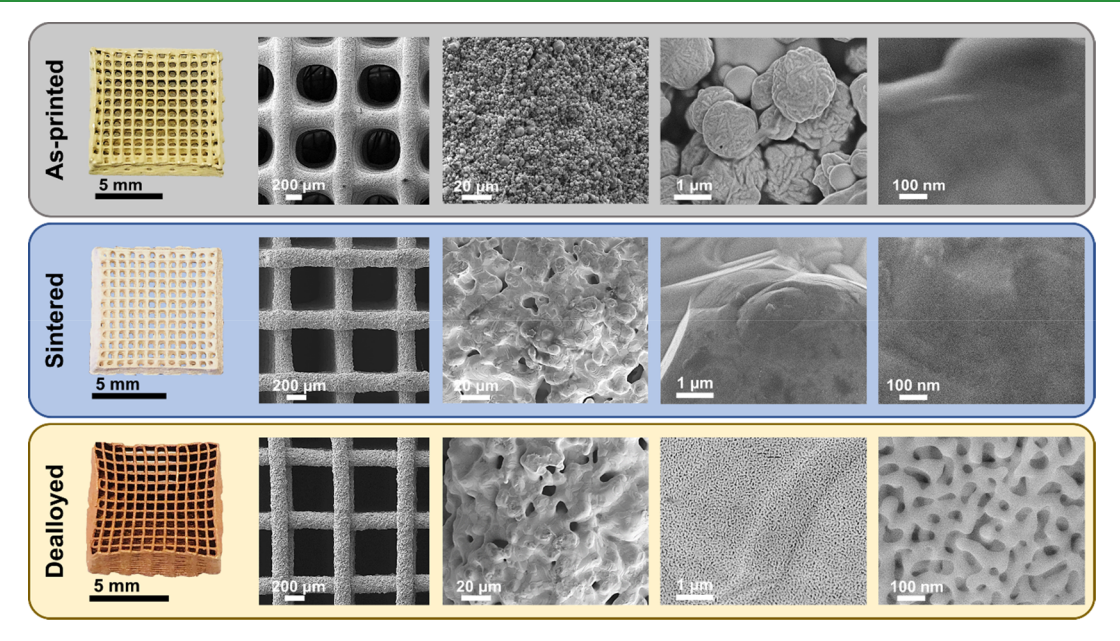


Figure 2. Photograms and SEM images of hierarchical porous Au (HP-Au) at different processing stages. The as-printed sample (first row) is composed of Au- and Ag-mixed powders, polymer binders, and solvents. Direct ink writing digitally dictates the macroscale porosity. The sintered sample (second row) is composed of alloyed Au and Ag, and microscale porosity arises from the evaporation of solvents and decomposition of polymer binder. Finally, Ag is selectively removed in the dealloyed sample (third row) to yield nanoscale porosity.

rate of 50 sccm and stirred at 300 rotations/min. All gaseous products were passed into a customized gas chromatography system (GC, Scion 456) equipped with a pulsed discharge detector (PDD) and a 5 Å molecular sieve-packed column. Helium gas (Airgas, 99.9999%) was used as carrier gas. The partial current densities of CO and H<sub>2</sub> were derived from the GC peak area using the following equations:<sup>31</sup>

$$j_{\rm CO} = \frac{{\rm peak~area}}{\alpha} \times {\rm flow~rate} \times \frac{2Fp_0}{RT} \times ({\rm electrode~area})^{-1}$$
 (1)

$$j_{\rm H_2} = \frac{\rm peak~area}{\beta} \times {\rm flow~rate} \times \frac{2Fp_0}{RT} \times ({\rm electrode~area})^{-1}$$
 (2)

where F is Faraday's constant,  $p_0 = 1.013$  bar, R is the gas constant, Tis the room temperature (293.15 K), and  $\alpha/\beta$  are the conversion factors for CO and H2 based on gas standards with known concentration.

# 3. RESULTS AND DISCUSSION

3.1. Ink Viscosity. The viscosity of the raw Au and Ag clays is too high to mix and print. The addition of a solvent enables the mixing and formation of Au-Ag composite inks with homogeneous, gel-like behavior that gives rise to excellent printability. Figure 1 shows the rheological properties of the

Au-Ag ink. The apparent viscosity of the ink decreases as the applied shear rate increases (Figure 1a), which shows the shear-thinning properties of the ink. This shear-thinning property allows the ink to flow readily when a shear stress is applied. Figure 1b depicts the storage (G') and loss (G'')moduli of the ink, plotted against the applied shear stress. The storage modulus represents the ability of the ink to store energy via elastic deformation which describes the elastic response of the material, while the loss modulus represents the ink's ability to dissipate energy during deformation which illustrates the viscous response of the material. When the applied shear stress exceeds 70 Pa, the storage modulus falls below the loss modulus, and the ink will act more as a liquid and will flow through the nozzle. After the ink exits the nozzle, it no longer experiences any shear stress, and the storage and loss moduli recover such that the ink acts as a solid. Thus, the extruded filaments can hold their shape and support the 3Dprinted structure.

3.2. Structural Characterization of Fabricated Materials. 3.2.1. Hierarchical 3D-Printed Architecture. The typical morphology of the fabricated HP-Au samples at different processing stages is compiled in Figure 2. Three levels of

porosity can be observed: 32,33 (i) Macroscale pores with size  $\approx$ 500  $\mu$ m are shown in the second column and first, second, and third rows. These macroscale pores arise from direct ink writing. The shape of the macroscale pores is near-spherical after printing but becomes square after sintering because of the loss of organic binder, which leads to large shrinkage during sintering and creates thin straight filaments of fully sintered Au-Ag solid solution alloy. (ii) Microscale pores with size  $\approx 1$ 10  $\mu$ m are shown in the third column and second and third rows. These microscale pores are not present in as-printed samples (first row, Figure 2) because they arise from solvent evaporation and polymer binder decomposition during the sintering step (second row, Figure 2). (iii) Nanoscale pores with size of  $\approx$ 50 nm are shown at a low magnification in the fourth column third row, and at a high magnification in the fifth column third row. These nanoscale pores arise from Ag removal during dealloying. Note that the microscale pores from step (ii) are preserved during the dealloying step (third column third row, Figure 2). We anticipate that the coexistence of macroscale and microscale pores will facilitate the mass transport,<sup>34</sup> while the nanoscale ligaments and pores will provide a large surface area and active catalytic sites for the  $CO_2$  reduction reaction to take place.<sup>35</sup> In contrast, the 6  $\mu$ mthick NP-Au used for control experiments only exhibits unimodal porosity with an average ligament size of ≈41 nm (Figure S1).

3.2.2. Chemical Composition. The composition of the fabricated materials investigated at various processing stages was estimated by EDS to be Au<sub>31</sub>Ag<sub>69</sub> at.% after sintering, which is close to the targeted composition of Au<sub>30</sub>Ag<sub>70</sub> at.%. After dealloying, the composition changes from Au<sub>31</sub>Ag<sub>69</sub> to Au<sub>93</sub>Ag<sub>7</sub> at.%, which indicates that most of the sacrificial Ag were dissolved in HNO<sub>3</sub> during free corrosion dealloying. The composition of the 6  $\mu$ m-thick sample used for control experiments was Au<sub>27</sub>Ag<sub>73</sub> at.% before dealloying and Au<sub>97</sub>Ag<sub>3</sub> at.% after dealloying. Therefore, the HP-Au and NP-Au samples possessed a similar composition after dealloying. It should be noted that the ≈5 at.% residual Ag atoms exhibit lower catalytic activities compared to Au atoms, thus their contribution toward CO<sub>2</sub>-to-CO reduction can be ignored.<sup>35</sup>

3.2.3. Crystal Structure and Average Ligament Size. The crystal structure and nanoscale ligament size of the fabricated samples after sintering and dealloying were investigated using XRD and SAXS. Typical XRD patterns are shown in Figure 3a in black for sintered Au-Ag parent alloys, and in green for the corresponding HP-Au after dealloying. The two XRD patterns match very well with the face-centered cubic (FCC) crystal structure, which is expected since Au-Ag alloys and pure Au crystalize in the FCC structure. A peak broadening is observed on the XRD pattern of dealloyed samples as illustrated in the inset of Figure 3a by the magnified (111) peak shown in black (before dealloying) and in green (after dealloying). This peak broadening suggests the existence of nanoscale features in HP-Au. 36

Next, we used SAXS to further confirm the presence of nanoscale structures after dealloying.<sup>24,25</sup> Two typical SAXS patterns collected on a sintered Au-Ag parent alloy and the corresponding dealloyed HP-Au are shown in black and green in Figure 3b, respectively. The absence of a scattering peak on the SAXS pattern of the sintered sample (black) indicates that it is not porous at the nanoscale. 24-26 On the other hand, the SAXS pattern of the dealloyed HP-Au (green) shows a clear scattering peak centered around  $q \approx 0.008 \text{ Å}^{-1}$  in the q-space.

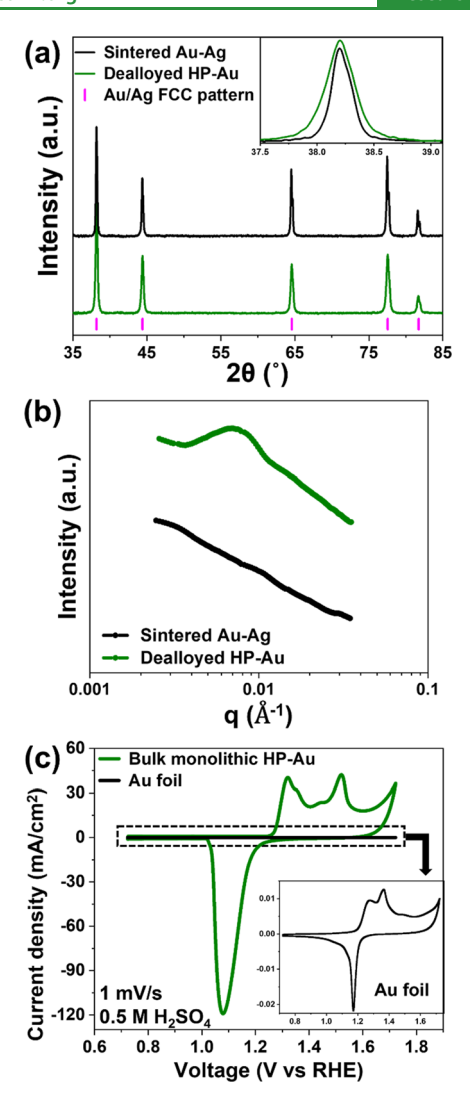


Figure 3. (a) XRD patterns of sintered Au-Ag (black) and dealloyed HP-Au (green), both matching the FCC pattern. The inset shows peak broadening in dealloyed HP-Au owing to the evolution of nanoscale morphology. (b) SAXS patterns of sintered Au-Ag (black) vs dealloyed HP-Au (green). The absence of scattering peaks in sintered Au-Ag suggests the absence of nanoscale porosity, while the dealloyed HP-Au shows a peak centered around the q-value of 0.008  ${\rm \AA}^{-1}$ . This corresponds to a ligament-to-ligament distance of  $\approx$ 97 nm. (c) CV profiles for Au foil (black) and dealloyed HP-Au (green) scanned under 1 mV/s, with the inset showing a magnified profile for

This peak position in the q-space can be converted to a characteristic size (d) in the real space using the following relation 24-26

$$d = 1.23 \times (2\pi/q) \tag{3}$$

In doing so, eq 3 yields a characteristic size  $d \approx 97 \pm 11$  nm, which corresponds to the ligament-ligament distance.<sup>24–26</sup> The error of ±11 nm is estimated from the broadening of the scattering peak. The average ligament size  $(d_1)$  is approximately half of the ligament-ligament distance, namely  $d_{\rm L} \approx 49$  $\pm$  6 nm. <sup>24–26</sup> This structure size of 49 nm determined from SAXS data agrees with the ≈50 nm directly estimated from SEM images (e.g., fifth column third row in Figure 2). It should be noted that despite the hierarchical porosity shown in Figure 2, only one scattering peak associated with nanoscale

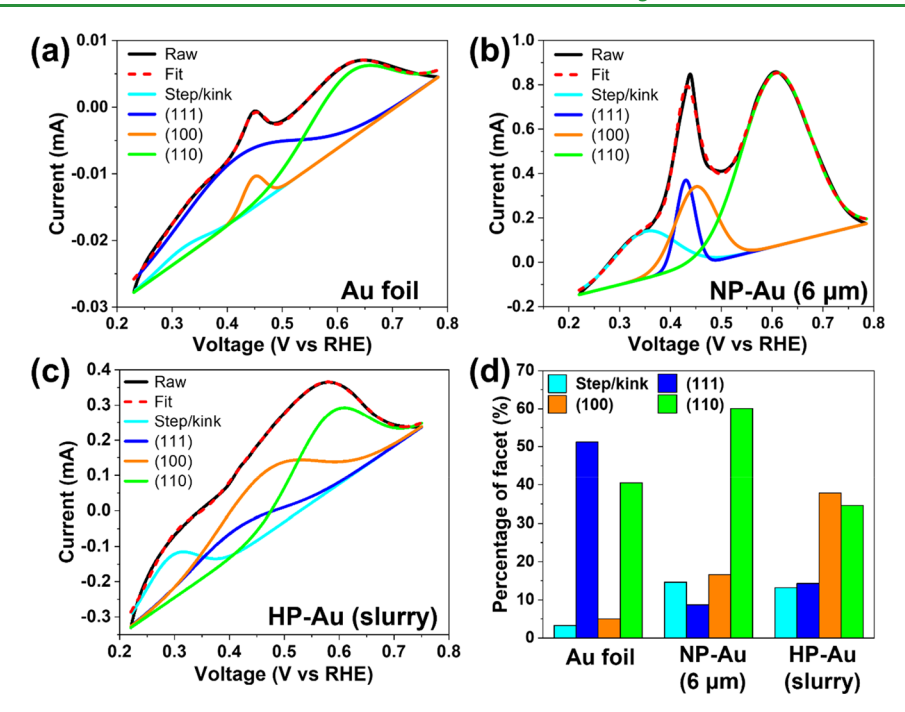


Figure 4. Peak deconvolution profiles for Pb underpotential deposition (Pb-UPD) of Au foil (a), 6  $\mu$ m-thick NP-Au (b), and HP-Au slurry (c) in 0.1 M NaOH + 1 mM Pb(ClO<sub>4</sub>)<sub>2</sub> solution. Scan rate: 20 mV/s. (d) Percentages of different facets.

ligaments and pores was observed. Scattering peaks associated with the macroscale and microscale pores were not observed because the sizes of these large pores are beyond the detection limit of our lab-scale X-ray scattering system.<sup>24</sup>

3.2.4. Surface Area and Surface-Active Facets Distribution. The specific surface area associated with the nanoscale ligaments in dealloyed HP-Au was estimated using the following relation: <sup>37–41</sup>

$$S = C/\rho d_{\rm I} \tag{4}$$

where  $\rho$  is the bulk density of Au (19.3 g/cm³),  $d_{\rm L}$  is the average ligament size (49 nm from SAXS), and C is a dimensionless constant associated with the shape of the pores. For disordered nanoporous metals, the value of C has been reported to be 3.7. Using eq 4, the specific surface area is calculated to be 4.0 m²/g which matches very well with typical values reported in the literature for the specific surface area of NP-Au with a comparable ligament size. Using the massnormalized surface area from eq 4, we found that the specific surface area per footprint area of our HP-Au samples is  $\approx 1.61 \times 10^4 \ {\rm cm}^2/{\rm cm}^2$ . This value will be used later to quantify the specific ECR activities.

Next, the electrochemical signature of the HP-Au investigated using CV techniques (green, Figure 3c) was found to be consistent with that of planar Au foil (black, inset Figure 3c), with a significant enhancement in the geometric current density ( $\approx\!6000$  times based on reduction peak height) originating from the enhanced specific surface area per footprint area. In addition, CV tests were also used to estimate the EASA per footprint area of dealloyed HP-Au. In doing so, we derived the ratio of the reduction charge density (i.e., specific capacity) between dealloyed HP-Au and planar Au foil under the same scan rate. <sup>29</sup> At the scan rate of 1 mV/s (Figure 3c), the dealloyed HP-Au yielded an EASA per footprint area of  $1.59\times10^4~\text{cm}^2/\text{cm}^2$  (detailed calculation is provided in the Supporting Information). This value agrees with the specific surface area per footprint area derived above. On the other

hand, CV scans at faster rates (i.e., 10 mV/s, Figure S2) yielded a decreased EASA per footprint area of  $1.23 \times 10^4$  cm²/cm², suggesting the robust HP-Au electrodes will suffer from mass transport limitation (diffusion of protons, adsorbed sulfate anions involved in the surface reaction, etc.).<sup>42</sup> This mass transport limitation is expected to significantly affect the ECR performance as will be discussed later.

It is well-established that the enhanced catalytic activities toward CO2-to-CO reduction in nanoporous metals not only arise from the increased surface area but also from the increased density of catalytic active sites such as high-index facets, steps, and kinks, which can effectively lower the energy barrier for CO<sub>2</sub>-to-CO reaction. 35,43,44 Therefore, in addition to the surface area discussed above, Pb underpotential deposition (Pb-UPD) was performed to study the exposed facets (Figure 4). Pb-UPD is a powerful tool for surface study since the deposition of Pb monolayer is sensitive to local order (facets), 45 and this technique has been widely used in NP-Au analysis. 30,46,47 Figure 4a-c shows the Pb desorption voltammetry profiles of Au foil, 6 µm NP-Au thin film, and dealloyed HP-Au, respectively. It should be noted that in Figure 4c, an HP-Au slurry electrode (Figure S3) consisting of HP-Au particles, conductive carbon, and PVDF binder was used instead of a monolithic HP-Au. This is because usually fast CV scans, 20 mV/s in our case, are applied in UPD in order to obtain monolayer plating/stripping and avoid a bulk deposition. 48 However, due to the bulk nature (mm-scale thickness) and sluggish diffusion kinetics of the monolithic HP-Au sample, characteristic plating/stripping peaks could not be observed under such fast scan rates as shown in Figure S4. Based on previous reports, the Pb stripping profile can be deconvoluted into four peaks: step/kinks with a peak at ≈0.30 V vs RHE, (111) facets with a peak at  $\approx$ 0.41 V vs RHE, (100) facets with a peak at ≈0.45 V vs RHE, and last (110) facets with a strong peak at ≈0.60 V vs RHE. 46,47 Figure 4d summarizes the fraction of facets in different samples: in dealloyed samples, the ratio of step/kink is 14.6% for 6  $\mu$ m

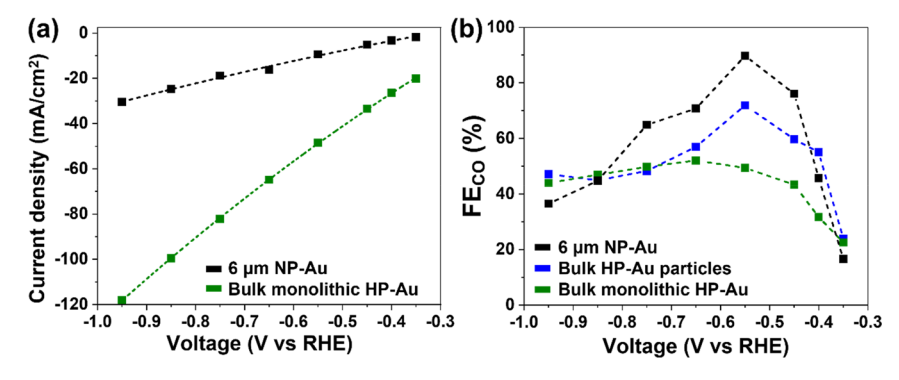


Figure 5. (a) Geometric current density was obtained at different reduction potentials for 6 μm NP-Au (black) and monolithic HP-Au (green). The dots represent collected data, and the dashed curves represent fitting. (b) CO Faradaic efficiency (FE) as a function of applied potential for 6 μm NP-Au (black), HP-Au particles (blue), and monolithic HP-Au (green).

Table 1. Overview of the Performances of Various Au-Based Electrocatalysts toward CO<sub>2</sub>-to-CO Reduction

material category	electrode description	potential (V vs RHE)	$j_{\rm CO} \left({\rm mA/cm}^2\right)$	j <sub>CO</sub> (mA/mg)	CO selectivity	reference
industrial requirement			>190	>100	>95%	18
HP-Au	monolithic HP-Au	-0.65	33.8	0.05	52%	this work
	HP-Au sealed in acrylic casing	-0.55	5.0	N/A	70%	34
	HP-Au (4.4 $\mu$ m thick) on Si substrate	-0.57	5.2	3.3	92%	21
NP-Au thin film	monolithic NP-Au (6 $\mu$ m thick)	-0.55	8.4	2.6	90%	this work
	Monolithic NP-Au (25 $\mu$ m thick)	-0.5	11.8	N/A	98%	7
	monolithic NP-Au (200 $\mu$ m thick)	-0.39	5.9	N/A	98%	51
	NP-Au (664 nm thick) on Si substrate	-0.5	6.2	N/A	99%	12
Au nanoparticles (NPs)	20 mg Au NPs (8 nm) in slurry	-0.52	N/A	3.0	97%	6
	Au NPs (20–40 nm) grown on Au foil with 1–2 $\mu$ m thickness	-0.4	9.8	N/A	98%	11
	0.2 mg Au NPs (18 nm) on carbon nanotube	-0.5	N/A	15.0	94%	9

NP-Au and 13.2% for HP-Au, both are  $\approx$ 4 times of that in planar Au foil (3.3%). This result suggests that compared to their planar counterparts, both 6  $\mu$ m NP-Au and HP-Au can be expected to achieve a superior performance toward ECR not only because of the enhanced surface area but also due to enriched surface catalytic sites. It should be noted that the difference in the fraction of other facets, for instance (111) rich in Au foil and (110) rich in 6  $\mu$ m NP-Au, comes from the way the materials are processed into a thin film (cold rolling and/or beating), <sup>22,49</sup> while the contribution of these facets toward ECR is minor compared to high-index facets, steps, and kinks. <sup>35</sup>

3.3. CO<sub>2</sub>-to-CO Reduction. 3.3.1. Current Density and Selectivity. CO2-to-CO reduction tests were performed on monolithic HP-Au ( $\approx$ 150 mg) and a 6  $\mu$ m-thick NP-Au film (control sample) using an H-cell: A schematic setup with halfcell reactions and a picture of the actual cell are shown in Figure S5.50 The typical current densities recorded on these two samples as a function of the applied potential are shown in green (for monolithic HP-Au) and black (for 6 µm-thick NP-Au) in Figure 5a. At high overpotentials (below -0.85 V vs RHE), the current density of the monolithic HP-Au exceeds 100 mA/cm<sup>2</sup>, which is  $\approx$ 4 times higher than that of the 6  $\mu$ m NP-Au. However, the maximum selectivity (Faradaic efficiency (FE)) of the monolithic HP-Au is only  $\approx$ 52% at -0.65 V vs RHE (green curve, Figure 5b), which is lower than the 90% peak selectivity achieved in the 6 µm-thick NP-Au film at -0.55 V vs RHE (black curve, Figure 5b). For comparison, the performances of various Au-based electrocatalysts toward CO<sub>2</sub>to-CO reduction are summarized in Table 1 (to ensure a fair

comparison, only data from experiments carried out in aqueous electrolytes using H-cells are listed in Table 1). It is seen that under a similar overpotential, the monolithic HP-Au delivers a CO partial current density of ≈33.8 mA/cm<sup>2</sup>, which is one order of magnitude higher than the typical CO partial current density achieved using nanostructured Au electrode materials. On the other hand, the selectivity of 52% achieved in monolithic HP-Au is lower than the minimum 95% selectivity desirable for practical industrial applications. This relatively low selectivity originates from mass transport limitations. Detailed discussion on mass transport restrictions is provided in the Supporting Information. To verify that mass transport is indeed responsible for the low selectivity, the monolithic HP-Au with bulk dimension of  $\approx 200 \ \mu m$  (measured by the 3Dprinted wall thickness, see Figure 2) was ground into particles to reduce the bulk dimension from  $\approx$ 200  $\mu$ m down to  $\approx$ 50  $\mu$ m (i.e., 4 times decrease in bulk dimension). These bulk HP-Au particles were then mixed with conductive carbon and PVDF binder to prepare an HP-Au slurry electrode (Figure S3). The HP-Au particles achieved a selectivity of 72% at -0.55 V vs RHE (blue curve, Figure 5b), which corresponds to a 20% increase in selectivity compared to the monolithic HP-Au. It should be noted that in calculating the FE of HP-Au particles, the contribution of conductive carbon and PVDF binder in the slurry cathode was separately measured and subtracted, as those components only contributed to HER (Figure S6).

3.3.2. Specific ECR Activity. We then investigated the effect of surface area on the current density trends for the three electrocatalysts with three different bulk dimensions, namely  $\approx 6$ , 50, and 200  $\mu$ m, respectively. Figure 6a shows the

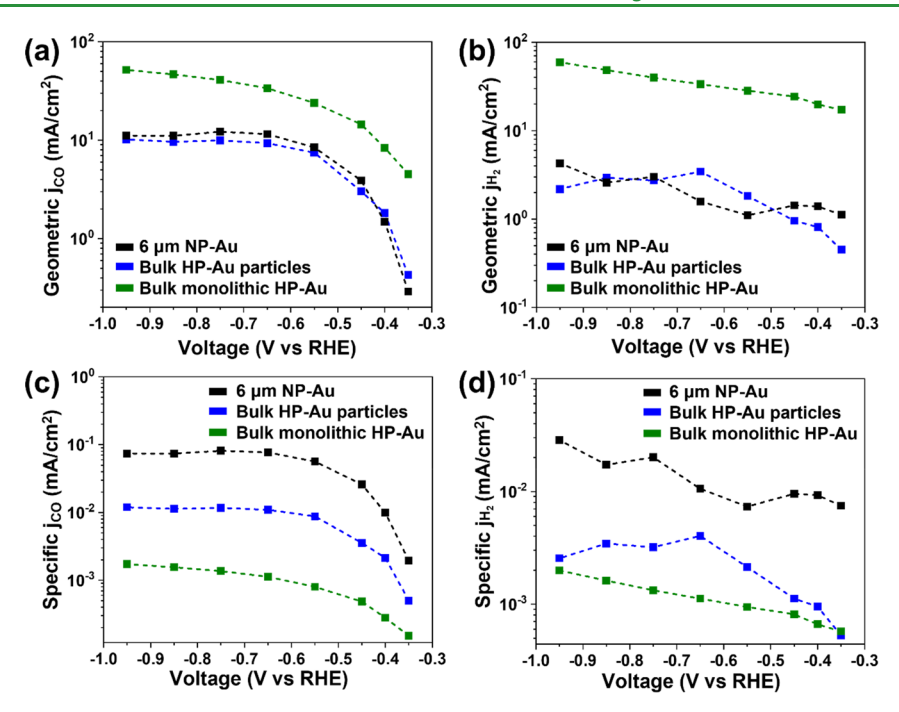


Figure 6. Geometric current density of CO (a) and H<sub>2</sub> (b), and specific current density of CO (c) and H<sub>2</sub> (d) as a function of applied potential for 6 μm NP-Au (black), HP-Au particles (blue), and monolithic HP-Au (green). The specific current densities are derived from the specific surface area.

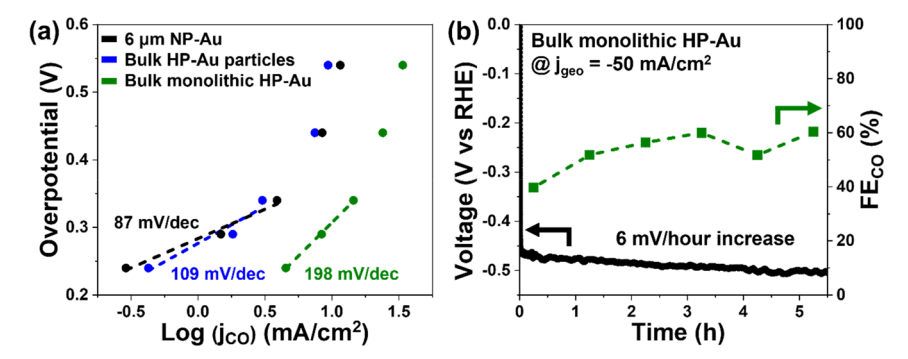


Figure 7. (a) Tafel slope analysis for  $6 \mu m$  NP-Au (black), HP-Au particles (blue), and monolithic HP-Au (green). (b) Stability test for monolithic HP-Au at a constant current density of 50 mA/cm<sup>2</sup> (black), with CO Faradaic efficiency (FE) measured every 60 min (green).

geometric current densities associated with CO formation, and Figure 6b shows the corresponding geometric current densities associated with the competing H<sub>2</sub> evolution. It is seen that the monolithic HP-Au with bulk dimension 200  $\mu$ m exhibits the highest geometric current densities for both CO and H<sub>2</sub> formation. The specific current density, derived from normalizing the geometric current with respect to the specific surface area, can provide insight into the origin of ECR activity.<sup>3</sup> Figure 6c shows the specific current densities associated with CO formation, and Figure 6d shows the corresponding specific current densities associated with the competing H<sub>2</sub> evolution. Despite exhibiting the highest geometric current density, the monolithic HP-Au displayed only ≈1% of specific CO activity and  $\approx$ 10% of specific H<sub>2</sub> activity compared to the 6  $\mu$ m NP-Au. Due to the similar nanoscale morphology observed under SEM (Figures 2 and S1) and a similar fraction of step/kink observed under Pb-UPD (Figure 4), it should be expected that the two materials exhibit similar catalytic properties. Thus, we postulate the significant decrease in specific activity in monolithic HP-Au originates from the mass transport limitations. Specifically, a number of active catalytic sites in

the bulk cannot be effectively accessed owing to the slow diffusion of reaction species. Interestingly, the HP-Au particles showed improved specific activities compared to monolithic HP-Au, with an enhancement of  $\approx 11$  times for CO and  $\approx 2.3$ times for  $H_2$  at -0.55 V vs RHE. Since the HP-Au particles are identical in nature to monolithic HP-Au, with bulk dimension being the only difference, this result proves our speculation that the kinetic of mass transport in the monolithic HP-Au electrode is sluggish. Moreover, the increase in CO is ≈5 times that of H<sub>2</sub>, suggesting that the surface of HP-Au is highly active toward ECR as long as they can be accessed. It should be noted that despite the enhanced specific activities obtained in HP-Au particles, their values are still one order of magnitude lower compared with 6  $\mu$ m NP-Au, suggesting that the mass transport is improved but not entirely resolved. The comparative study here shows that bulk dimension is a critical parameter to be considered for the design of high-performance electrocatalysts. In the case of monolithic HP-Au, its bulk dimension (i.e., 3D-printed wall thickness) can be digitally controlled from  $\approx 100 \ \mu m$  to 1 mm by adjusting the nozzle size.

3.3.3. Tafel Analysis. Tafel slopes in ECR can be used to indicate the reaction pathway and rate-determining step. Therefore, the CO partial current densities in Figure 6a were further used to derive the Tafel slope (Figure 7a) for each sample. These Tafel slopes were found to be 87, 109, and 198 mV/dec for the three samples with bulk dimension of 6, 50, and 200  $\mu$ m, respectively. The Tafel slope of 87 mV/dec for 6  $\mu$ m NP-Au suggests a fast pre-equilibrium step (1 e Transfer to form CO<sub>2</sub> prior to the subsequent nonelectron-transfer rate-determining step; the Tafel slope of 109 mV/dec for HP-Au particles suggests the rate-determining step is the 1 e Transfer to form CO<sub>2</sub>-; finally, the Tafel slope of 198 mV/dec for monolithic HP-Au reflects the mass transport limitations.

3.3.4. Stability. Last, we investigated the stability of monolithic HP-Au. Figure 7b shows the galvanostatic ECR profile of monolithic HP-Au over 5.5 h, under a constant reduction current of 10 mA (corresponding to a geometric current density of 50 mA/cm²). The overall selectivity, neglecting the first 15 min where the system was still equilibrating, was stable between 50 and 60%, and the monolithic HP-Au showed slight degradation over time with an increase in overpotential of  $\approx 6$  mV/h.

# 4. CONCLUSIONS AND OUTLOOK

In summary, we used direct ink writing in combination with dealloying to design hierarchical porous Au structures for use as robust CO2-to-CO reduction electrocatalysts with enhanced mass transport enabled by the presence of three levels of porosity, namely macroscale pores ( $\approx 500 \mu m$ ), microscale pores  $(1-10 \mu m)$ , and nanoscale pores ( $\approx 50 \text{ nm}$ ). With the robust design of our hierarchical porous Au, a total current density of 64.9 mA/cm<sup>2</sup> with a CO partial current density of 33.8 mA/cm<sup>2</sup> is achieved in H-cell configuration under an overpotential of 0.55 V. This current density is one order of magnitude higher than those commonly reported in conventional nanostructured materials. On the other hand, the relatively low selectivity of 52% was proven to arise from sluggish mass transport, which remains a critical issue despite the hierarchical architecture. The insights gained in this work can navigate us toward a better design of electrocatalysts, taking advantage of the design flexibility of additive manufacturing and dealloying.<sup>53</sup> For instance, the macroscale 3D-printed wall thickness can be digitally controlled by adjusting the nozzle size.<sup>33</sup> In addition, the size and density of microscale pores can be adjusted by tuning the ratio between metal powders and polymer binders in the starting ink. Finally, the degree of nanoporosity can be tuned with various methods, including dealloying condition<sup>54</sup> and postdealloying treatment.<sup>33</sup> The synergy among the multiscale features shall balance the reaction rate and selectivity, which paves the way for the future design of electrocatalysts toward scale-up applications.

# ASSOCIATED CONTENT

# Supporting Information

The Supporting Information is available free of charge at https://pubs.acs.org/doi/10.1021/acsami.3c02050.

SEM of 6  $\mu$ m NP-Au, CV tests of HP-Au and planer Au foil, SEM and EDS mapping of HP-Au slurry, UPD profiles of monolithic HP-Au and HP-Au slurry, schematic of H-type cell used for CO<sub>2</sub> reduction, gas chromatograph raw data, H<sub>2</sub> Faradaic efficiency for all

Au samples, calculation of electrochemically active surface area, and evaluation of mass transport (PDF)

# AUTHOR INFORMATION

## **Corresponding Authors**

Wen Chen – Department of Mechanical and Industrial Engineering, University of Massachusetts, Amherst, Massachusetts 01003-2210, United States; Email: wenchen@umass.edu

Eric Detsi — Department of Materials Science & Engineering, University of Pennsylvania, Philadelphia, Pennsylvania 19104-6272, United States; orcid.org/0000-0002-4009-7260; Email: detsi@seas.upenn.edu

## **Authors**

Jintao Fu — Department of Materials Science & Engineering, University of Pennsylvania, Philadelphia, Pennsylvania 19104-6272, United States

Shahryar Mooraj – Department of Mechanical and Industrial Engineering, University of Massachusetts, Amherst, Massachusetts 01003-2210, United States

Alexander K. Ng — Department of Materials Science & Engineering, University of Pennsylvania, Philadelphia, Pennsylvania 19104-6272, United States; orcid.org/0000-0002-3227-9582

Cheng Zhu — Lawrence Livermore National Laboratory, Livermore, California 94550, United States; orcid.org/ 0000-0003-0084-1099

Complete contact information is available at: https://pubs.acs.org/10.1021/acsami.3c02050

# **Author Contributions**

J.F. and S.M. contributed equally.

### Notes

The authors declare no competing financial interest.

## ACKNOWLEDGMENTS

The authors gratefully acknowledge the National Science Foundation (NSF) for their financial support through the NSF-CAREER CMMI-2047851 (E.D.), NSF FM-2134715 (W.C.), MRSEC DMR-1720530, and NSF MRI-1725969. The NSF MRI-1725969 grant was used to acquire the XENOCS Xeuss 2.0 Dual Cu-Mo source and Environmental X-ray Source (DEXS) used in this research. This work was supported by Lawrence Livermore National Laboratory under the auspices of the US Department of Energy under Contract DE-AC52-07NA27344, IM release No: LLNL-JRNL-848804. This work was performed in part at the Singh Center for Nanotechnology at the University of Pennsylvania, a member of the National Nanotechnology Coordinated Infrastructure (NNCI) network, which is supported by the National Science Foundation (Grant NNCI-1542153). The authors are thankful to Shuai Feng for his contributions to the ink preparation and thermal sintering protocol development.

## REFERENCES

- (1) Wang, Y.; Han, P.; Lv, X.; Zhang, L.; Zheng, G. Defect and Interface Engineering for Aqueous Electrocatalytic CO2 Reduction. *Joule* **2018**, 2, 2551–2582.
- (2) Sun, D.; Xu, X.; Qin, Y.; Jiang, S. P.; Shao, Z. Rational Design of Ag-Based Catalysts for the Electrochemical CO2 Reduction to CO: A Review. *ChemSusChem* **2020**, *13*, 39–58.

- (3) Hall, A. S.; Yoon, Y.; Wuttig, A.; Surendranath, Y. Mesostructure-Induced Selectivity in CO2 Reduction Catalysis. *J. Am. Chem. Soc.* **2015**, *137*, 14834–14837.
- (4) Hori, Y. Electrochemical CO<sub>2</sub> Reduction on Metal Electrodes. In *Modern Aspects of Electrochemistry*; Springer: New York, NY, 2008, 42, 89 –189.
- (5) Liu, H.; Zhu, Y.; Ma, J.; Zhang, Z.; Hu, W. Recent Advances in Atomic-Level Engineering of Nanostructured Catalysts for Electrochemical CO2 Reduction. *Adv. Funct. Mater.* **2020**, *30*, No. 1910534.
- (6) Zhu, W.; Michalsky, R.; Metin, O.; Lv, H.; Guo, S.; Wright, C. J.; Sun, X.; Peterson, A. A.; Sun, S. Monodisperse Au Nanoparticles for Selective Electrocatalytic Reduction of CO2 to CO. *J. Am. Chem. Soc.* **2013**, *135*, 16833–16836.
- (7) Lu, X.; Yu, T.; Wang, H.; Qian, L.; Lei, P. Electrochemical Fabrication and Reactivation of Nanoporous Gold with Abundant Surface Steps for CO2 Reduction. ACS Catal. 2020, 10, 8860–8869.
- (8) Sharma, P. P.; Wu, J.; Yadav, R. M.; Liu, M.; Wright, C. J.; Tiwary, C. S.; Yakobson, B. I.; Lou, J.; Ajayan, P. M.; Zhou, X.-D. Nitrogen-Doped Carbon Nanotube Arrays for High-Efficiency Electrochemical Reduction of CO2: On the Understanding of Defects, Defect Density, and Selectivity. *Angew. Chem., Int. Ed.* **2015**, *54*, 13701–13705.
- (9) Feng, X.; Jiang, K.; Fan, S.; Kanan, M. W. Grain-Boundary-Dependent CO2 Electroreduction Activity. *J. Am. Chem. Soc.* **2015**, 137, 4606–4609.
- (10) Kim, D.; Resasco, J.; Yu, Y.; Asiri, A. M.; Yang, P. Synergistic Geometric and Electronic Effects for Electrochemical Reduction of Carbon Dioxide Using Gold—Copper Bimetallic Nanoparticles. *Nat. Commun.* **2014**, *5*, 4948.
- (11) Chen, Y.; Li, C. W.; Kanan, M. W. Aqueous CO2 Reduction at Very Low Overpotential on Oxide-Derived Au Nanoparticles. *J. Am. Chem. Soc.* **2012**, *134*, 19969–19972.
- (12) Welch, A. J.; DuChene, J. S.; Tagliabue, G.; Davoyan, A.; Cheng, W.-H.; Atwater, H. A. Nanoporous Gold as a Highly Selective and Active Carbon Dioxide Reduction Catalyst. *ACS Appl. Energy Mater.* **2019**, *2*, 164–170.
- (13) Lee, C.-Y.; Zhao, Y.; Wang, C.; Mitchell, D. R. G.; Wallace, G. G. Rapid Formation of Self-Organised Ag Nanosheets with High Efficiency and Selectivity in CO2 Electroreduction to CO. *Sustain. Energy Fuels* **2017**, *1*, 1023–1027.
- (14) Hsieh, Y.-C.; Senanayake, S. D.; Zhang, Y.; Xu, W.; Polyansky, D. E. Effect of Chloride Anions on the Synthesis and Enhanced Catalytic Activity of Silver Nanocoral Electrodes for CO2 Electroreduction. ACS Catal. 2015, 5, 5349–5356.
- (15) Won, D. H.; Shin, H.; Koh, J.; Chung, J.; Lee, H. S.; Kim, H.; Woo, S. I. Highly Efficient, Selective, and Stable CO2 Electroreduction on a Hexagonal Zn Catalyst. *Angew. Chem., Int. Ed.* **2016**, *55*, 9297–9300.
- (16) Luo, W.; Zhang, J.; Li, M.; Züttel, A. Boosting CO Production in Electrocatalytic CO2 Reduction on Highly Porous Zn Catalysts. *ACS Catal.* **2019**, *9*, 3783–3791.
- (17) Hui, S.(. R.; Shaigan, N.; Neburchilov, V.; Zhang, L.; Malek, K.; Eikerling, M.; Luna, P. D. Three-Dimensional Cathodes for Electrochemical Reduction of CO2: From Macro- to Nano-Engineering. *Nanomaterials* **2020**, *10*, 1884.
- (18) Masel, R. I.; Liu, Z.; Yang, H.; Kaczur, J. J.; Carrillo, D.; Ren, S.; Salvatore, D.; Berlinguette, C. P. An Industrial Perspective on Catalysts for Low-Temperature CO2 Electrolysis. *Nat. Nanotechnol.* **2021**, *16*, 118–128.
- (19) Li, M.; Yan, C.; Ramachandran, R.; Lan, Y.; Dai, H.; Shan, H.; Meng, X.; Cui, D.; Wang, F.; Xu, Z.-X. Non-Peripheral Octamethyl-Substituted Cobalt Phthalocyanine Nanorods Supported on N-Doped Reduced Graphene Oxide Achieve Efficient Electrocatalytic CO2 Reduction to CO. Chem. Eng. J. 2022, 430, No. 133050.
- (20) Sun, Z.; Ma, T.; Tao, H.; Fan, Q.; Han, B. Fundamentals and Challenges of Electrochemical CO2 Reduction Using Two-Dimensional Materials. *Chem* **2017**, *3*, 560–587.
- (21) Gayea, H.; Tae, S. J.; Changui, A.; Youngjin, H.; Donghwi, C.; Jihun, O.; Seokwoo, J. Hierarchically Porous Au Nanostructures with

- Interconnected Channels for Efficient Mass Transport in Electrocatalytic CO2 Reduction. *Proc. Natl. Acad. Sci. U. S. A.* **2020**, 117, 5680–5685.
- (22) Ding, Y.; Kim, Y.-J.; Erlebacher, J. Nanoporous Gold Leaf: "Ancient Technology"/Advanced Material. *Adv. Mater.* **2004**, *16*, 1897–1900.
- (23) Mallard, W. C.; Gardner, A. B.; Bass, R. F.; Slifkin, L. M. Self-Diffusion in Silver-Gold Solid Solutions. *Phys. Rev.* **1963**, *129*, 617–625.
- (24) Welborn, S. S.; Detsi, E. Small-Angle X-Ray Scattering of Nanoporous Materials. *Nanoscale Horizons* **2020**, *5*, 12–24.
- (25) Ng, A. K.; Welborn, S. S.; Detsi, E. Time-Dependent Power Law Function for the Post-Dealloying Chemical Coarsening of Nanoporous Gold Derived Using Small-Angle X-Ray Scattering. *Scr. Mater.* **2022**, *206*, No. 114215.
- (26) Fu, J.; Corsi, J. S.; Welborn, S. S.; Basile, V.; Wang, L.; Ng, A. K.; Detsi, E. Eco-Friendly Synthesis of Nanoporous Magnesium by Air-Free Electrolytic Dealloying with Recovery of Sacrificial Elements for Energy Conversion and Storage Applications. *ACS Sustainable Chem. Eng.* **2021**, *9*, 2762–2769.
- (27) Lee, T.; Koh, H.; Ng, A. K.; Liu, J.; Stach, E. A.; Detsi, E. Ultrafine Nanoporous Aluminum by Electrolytic Dealloying of Aluminum-Magnesium Alloys in Glyme-Based Electrolytes with Recovery of Sacrificial Magnesium. *Scr. Mater.* **2022**, 221, No. 114959.
- (28) Welborn, S. S.; Corsi, J. S.; Wang, L.; Lee, A.; Fu, J.; Detsi, E. Effects of Side Reactions on the Kinetics of Nanoporous Gold Formation Revealed by Real-Time X-Ray Scattering during Electrolytic Dealloying. *J. Mater. Chem. A* **2021**, *9*, 19994–20005.
- (29) Rouya, E.; Cattarin, S.; Reed, M. L.; Kelly, R. G.; Zangari, G. Electrochemical Characterization of the Surface Area of Nanoporous Gold Films. *J. Electrochem. Soc.* **2012**, *159*, K97–K102.
- (30) Wang, M.; Meng, A.; Fu, J.; Foucher, A.; Serra-Maia, R.; Stach, E.; Detsi, E.; Pikul, J. Surface Facet Engineering in Nanoporous Gold for Low-Loading Catalysts in Aluminum—Air Batteries. ACS Appl. Mater. Interfaces 2021, 13, 13097—13105.
- (31) Li, J.; Chen, G.; Zhu, Y.; Liang, Z.; Pei, A.; Wu, C.-L.; Wang, H.; Lee, H. R.; Liu, K.; Chu, S.; Cui, Y. Efficient Electrocatalytic CO2 Reduction on a Three-Phase Interface. *Nat. Catal.* **2018**, *1*, 592–600.
- (32) Mooraj, S.; Welborn, S. S.; Jiang, S.; Peng, S.; Fu, J.; Baker, S.; Duoss, E. B.; Zhu, C.; Detsi, E.; Chen, W. Three-Dimensional Hierarchical Nanoporous Copper via Direct Ink Writing and Dealloying. Scr. Mater. 2020, 177, 146–150.
- (33) Zhu, C.; Qi, Z.; Beck, V. A.; Luneau, M.; Lattimer, J.; Chen, W.; Worsley, M. A.; Ye, J.; Duoss, E. B.; Spadaccini, C. M.; Friend, C. M.; Biener, J. Toward Digitally Controlled Catalyst Architectures: Hierarchical Nanoporous Gold via 3D Printing. *Sci. Adv.* **2018**, *4*, No. eaas9459.
- (34) Qi, Z.; Hawks, S. A.; Horwood, C.; Biener, J.; Biener, M. M. Mitigating Mass Transport Limitations: Hierarchical Nanoporous Gold Flow-through Electrodes for Electrochemical CO2 Reduction. *Mater. Adv.* **2022**, *3*, 381–388.
- (35) Zhang, W.; He, J.; Liu, S.; Niu, W.; Liu, P.; Zhao, Y.; Pang, F.; Xi, W.; Chen, M.; Zhang, W.; Pang, S. S.; Ding, Y. Atomic Origins of High Electrochemical CO2 Reduction Efficiency on Nanoporous Gold. *Nanoscale* **2018**, *10*, 8372–8376.
- (36) Graf, M.; Ngô, B.-N. D.; Weissmüller, J.; Markmann, J. X-Ray Studies of Nanoporous Gold: Powder Diffraction by Large Crystals with Small Holes. *Phys. Rev. Mater.* **2017**, *1*, No. 076003.
- (37) Detsi, E.; Vuković, Z.; Punzhin, S.; Bronsveld, P. M.; Onck, P. R.; De Hosson, J. T. M. Fine-Tuning the Feature Size of Nanoporous Silver. *CrystEngComm* **2012**, *14*, 5402–5406.
- (38) Detsi, E.; De Jong, E.; Zinchenko, A.; Vuković, Z.; Vuković, I.; Punzhin, S.; Loos, K.; Ten Brinke, G.; De Raedt, H. A.; Onck, P. R.; De Hosson, J. T. M. On the Specific Surface Area of Nanoporous Materials. *Acta Mater.* **2011**, *59*, 7488–7497.
- (39) Wild, S.; Bäumer, M.; Risse, T. Thermal Activation of Nanoporous Gold for Carbon Monoxide Oxidation. *J. Phys. Chem.* C 2022, 126, 1770–1777.

- (40) Detsi, E.; Cook, J. B.; Lesel, B. K.; Turner, C. L.; Liang, Y.-L.; Robbennolt, S.; Tolbert, S. H. Mesoporous Ni60Fe30Mn10-Alloy Based Metal/Metal Oxide Composite Thick Films as Highly Active and Robust Oxygen Evolution Catalysts. *Energy Environ. Sci.* **2016**, *9*, 540–549.
- (41) Hakamada, M.; Kato, N.; Miyazawa, N.; Mabuchi, M. Water-Adsorption Effect on Electrical Resistivity of Nanoporous Gold. *Scr. Mater.* **2016**, *123*, 30–33.
- (42) Tan, Y. H.; Davis, J. A.; Fujikawa, K.; Ganesh, N. V.; Demchenko, A. V.; Stine, K. J. Surface Area and Pore Size Characteristics of Nanoporous Gold Subjected to Thermal, Mechanical, or Surface Modification Studied Using Gas Adsorption Isotherms, Cyclic Voltammetry, Thermogravimetric Analysis, and Scanning Electron Microscopy. *J. Mater. Chem.* 2012, 22, 6733–6745.
- (43) Fu, J.; Detsi, E.; De Hosson, J. T. M. Recent Advances in Nanoporous Materials for Renewable Energy Resources Conversion into Fuels. *Surf. Coat. Technol.* **2018**, 347, 320–336.
- (44) Lu, Q.; Rosen, J.; Zhou, Y.; Hutchings, G. S.; Kimmel, Y. C.; Chen, J. G.; Jiao, F. A Selective and Efficient Electrocatalyst for Carbon Dioxide Reduction. *Nat. Commun.* **2014**, *5*, 3242.
- (45) Mayet, N.; Servat, K.; Kokoh, K. B.; Napporn, T. W. Probing the Surface of Noble Metals Electrochemically by Underpotential Deposition of Transition Metals. *Surfaces* **2019**, *2*, 257–276.
- (46) Wang, Z.; Ning, S.; Liu, P.; Ding, Y.; Hirata, A.; Fujita, T.; Chen, M. Tuning Surface Structure of 3D Nanoporous Gold by Surfactant-Free Electrochemical Potential Cycling. *Adv. Mater.* **2017**, 29, No. 1703601.
- (47) Wang, Z.; Liu, P.; Han, J.; Cheng, C.; Ning, S.; Hirata, A.; Fujita, T.; Chen, M. Engineering the Internal Surfaces of Three-Dimensional Nanoporous Catalysts by Surfactant-Modified Dealloying. *Nat. Commun.* **2017**, *8*, 1066.
- (48) Zen, J.-M.; Yang, C.-C.; Senthil Kumar, A. Potential Scan Rate Dependence of Underpotential and Bulk Depositions of Lead on Screen-Printed Silver Electrodes. *Electrochim. Acta* **2001**, *47*, 899–904.
- (49) Fu, J.; Corsi, J. S.; Wang, Z.; Wei, H.; Detsi, E. Integrated Metal-Air Battery and Selective Electrolytic Leaching Cell for the Preparation of Nanoporous Metals. *ACS Appl. Nano Mater.* **2018**, *1*, 4164–4169.
- (50) Tufa, R. A.; Chanda, D.; Ma, M.; Aili, D.; Demissie, T. B.; Vaes, J.; Li, Q.; Liu, S.; Pant, D. Towards Highly Efficient Electrochemical CO2 Reduction: Cell Designs, Membranes and Electrocatalysts. *Appl. Energy* **2020**, *277*, No. 115557.
- (51) Qi, Z.; Biener, J.; Biener, M. Surface Oxide-Derived Nanoporous Gold Catalysts for Electrochemical CO2-to-CO Reduction. ACS Appl. Energy Mater. 2019, 2, 7717–7721.
- (52) Zhang, L.; Zhao, Z.-J.; Gong, J. Nanostructured Materials for Heterogeneous Electrocatalytic CO2 Reduction and Their Related Reaction Mechanisms. *Angew. Chem., Int. Ed.* **2017**, *56*, 11326–11353.
- (53) Mooraj, S.; Qi, Z.; Zhu, C.; Ren, J.; Peng, S.; Liu, L.; Zhang, S.; Feng, S.; Kong, F.; Liu, Y.; Duoss, E. B.; Baker, S.; Chen, W. 3D Printing of Metal-Based Materials for Renewable Energy Applications. *Nano Res.* **2021**, *14*, 2105–2132.
- (54) Detsi, E.; Van De Schootbrugge, M.; Punzhin, S.; Onck, P. R.; De Hosson, J. T. M. On Tuning the Morphology of Nanoporous Gold. *Scr. Mater.* **2011**, *64*, 319–322.